Int J Fract (2012) 178:179–194
DOI 10.1007/s10704-012-9778-z

ORIGINAL PAPER

A meso-mechanical model for concrete under dynamic tensile and compressive loading

L. Snozzi · F. Gatuingt · J. F. Molinari

Received: 20 January 2012 / Accepted: 15 October 2012 / Published online: 25 October 2012

Abstract We present a computational model, which combines interface debonding and frictional contact, in order to investigate the response of concrete specimens subjected to dynamic tensile and compressive loading. Concrete is modeled using a meso-mechanical approach in which aggregates and mortar are represented explicitly, thus allowing all material parameters to be physically identified. The material phases are considered to behave elastically, while initiation, coalescence and propagation of cracks are modeled by dynamically inserted cohesive elements. The impenetrability condition is enforced by a contact algorithm that resorts to the classical law of Coulomb friction. We show that the proposed model is able to capture the general increase in strength with increasing rate of loading and the tension/compression asymmetry. Moreover, we simulate compression with lateral confinement showing that the model reproduces the increase in peak strength with increasing confinement level. We also quantify the increase in the ratio between dissipated frictional energy and dissipated fracture energy as the confining pressure is augmented. Our results demonstrate the fundamental importance of capturing frictional mechanisms, which appear to dissipate a similar amount of energy when compared to cracking under compressive loading.

Keywords Cohesive zone model · Dynamic fracture · Concrete · Frictional contact · Meso-scale · Numerical methods

L. Snozzi · J. F. Molinari
Computational Solid Mechanics Laboratory (LSMS), School of Architecture, Civil and Environmental Engineering (ENAC), ÉCole Polytechnique Fédérale de Lausanne (EPFL), Bâtiment GC - A2, Station 18, 1015 Lausanne, Switzerland

F. Gatuingt (✉)
L.M.T. Cachan, 61 Avenue du Président Wilson, 94235 Cachan Cedex, France
e-mail: fabrice.gatuingt@ens-cachan.fr

1 Introduction

Failure of heterogeneous (quasi) brittle materials such as concrete is a complex and nonlinear phenomenon, which dissipates energy according to its (meso-structural) composition, geometry and loading conditions. Fracture of these materials involves the opening of local micro-cracks, which may propagate, coalesce and subsequently opposing crack surfaces enter into contact influencing the nonlinear failure process. Therefore, a careful treatment of both fracture and frictional mechanisms is needed in order to correctly reproduce the material's behavior.

The concrete constitutive behavior can be formulated either at the macro-scale or at the meso-scale. At the macro scale, the ingredients that characterize concrete's heterogeneity are not represented and one considers it as a homogeneous material. Therefore, in this case, the constitutive models need to have recourse to (visco)-plasticity coupled with a continuum damage

formulation (Ottosen 1979; Dubé et al. 1996; Sercombe et al. 1998; Bazant et al. 2000; Gatuingt and Pijaudier-Cabot 2002; Pedersen et al. 2008; Gatuingt et al. 2008; Desmorat et al. 2010; Pontiroli et al. 2010; Desmorat et al. 2010). This leads to models with a relatively high number of parameters, which are difficult to relate to physical mechanisms that occur during failure. On the contrary, a meso-scale level of observation (as proposed in Wittmann 1983) allows an explicit representation of some concrete constituents, which enables reducing the number of model parameters and to describe the interactions between matrix and inclusions. In the literature one can find several meso-scale models for concrete. They can be divided in two main computational classes. A first family is represented by lattice models (for instance Schlangen and van Mier 1992; Bolander and Saito 1998), where the continuum is replaced by a system of discrete particles and the mechanical properties of the lattice beams aim to represent the concrete meso-structure (Kozicki and Tejchman 2007; Grassl and Rempling 2008; Grassl and Jirásek 2010; Cusatis 2011). The second class resorts to the finite-element approach, in which concrete is usually represented as a biphasic material, made of a mixture of aggregates embedded in a matrix phase with an interfacial transition zone (ITZ) between them (Roelfstra et al. 1985; Vonk 1993; Cervenka et al. 1998; López 1999; Carol et al. 2001; Caballero et al. 2006; Snozzi et al. 2011; Gatuingt et al.).

The aim of this study is to exploit a 2D meso-mechanical finite-element model for analyzing failure of concrete specimens in compression. Our intention is to extend the mesoscopic approach that has been already applied to tensile loading in Snozzi et al. (2011), and Gatuingt et al.. To this end, a contact algorithm is included in the formulation to avoid interpenetration of the generated crack surfaces and allow mode II debonding of cohesive surfaces under the presence of (local) compression. The coupling between cohesive zone modeling and the impenetrability constraint is performed in an explicit dynamics scheme. This coupling has been already described in a previous work Snozzi and Molinari (2012), where it has been tested with a simple shearing problem, while in this paper it is applied to a more complex problem that involves a dense network of micro-cracks. The main characteristics of this model are a continuous transition from decohesion to pure frictional sliding (note that the onset of friction starts in conjunction with the onset of cracking). The debonding is controlled by an initially-rigid traction separation law (TSL), which enables us to define two separate values for the dissipated fracture energy in mode I and II. In this paper we will verify if the approach is able to reproduce the dissymmetric tensile/compressive behavior, strain rate strengthening and confinement effects. Comparison with experimental results is provided.

The paper is composed as follows. Section 2 describes the chosen finite element framework with frictional and cohesive capability for representing crack propagation. In Sect. 3 the meso-scale approach with its material parameters is presented. Results are reported in Sect. 4 for uniaxial tension and compression. While results on biaxial compressive loading are listed in Sect. 5. Finally, concluding remarks are stated in Sect. 6.

2 Numerical approach

The following section summarizes the formulation of the adopted frictional/cohesive capability for modeling crack propagation in FE including the adopted TSL, the selected contact enforcement algorithm and the coupling scheme between these two components. However, a more complete formulation and validation of the method can be found in Snozzi and Molinari (2012). The approach has been conceived for simulations in explicit dynamics (second order explicit version of the popular Newmark β-method Newmark 1959). This scheme is applied to the discretized equation of dynamic equilibrium:

$$\mathbf{M}\ddot{\mathbf{x}} + \mathbf{R}^{\mathbf{int}} = \mathbf{R}^{\mathbf{ext}} \tag{1}$$

where $\mathbf{M}$ represents the mass matrix, $\ddot{\mathbf{x}}$ the nodal acceleration vector and $\mathbf{R}^{\mathbf{ext}}$ and $\mathbf{R}^{\mathbf{int}}$ are the external and internal force vector respectively. The combination of a lumped mass matrix with the explicit scheme allows to trivially invert the mass matrix solving explicitly the scheme. Stability is achieved under the condition that the time step is below a critical value, which is

$$\Delta t_{crit} = \alpha \min_{1 \le e \le N_e} \left(\frac{l_e}{c} \right) \tag{2}$$

where c represents the plain strain compression stress wave speed and l_e is the size of the element. The stable time step has to be chosen equal to the smallest value over all elements (N_e) multiplied by a security

coefficient α (typically around 0.1). All the simulations presented thereafter have been conducted in a 2D plane strain configuration using mesh composed of six-noded quadratic triangles.

2.1 Cohesive approach

A well-known method to model the onset of fracture is to have recourse to cohesive zone modeling, which has been introduced by Dugdale (1960) and Barenblatt (1962) in the 1960s. This method describes fracture as a separation process by relating the displacement jump, which occurs at the crack tip, with tractions.

Within the computational framework this region (also called fracture process zone) is represented by interface elements with null thickness. While damage is concentrated in these elements, we will assume that the surrounding bulk material behaves linear elastically. The decohesion process is controlled by a constitutive relationship called traction separation law, which is usually related to a potential. Depending on the response of the cohesive surface prior softening behavior it is possible to distinguish between two main classes of TSL. The interface can exhibit an initial elastic behavior, intrinsic approach (e.g. Xu and Needleman 1993), or is assumed to be initially rigid, extrinsic approach (e.g. Camacho and Ortiz 1996). This second method implies that cohesive elements have to be inserted dynamically, avoiding the artificial compliance of the uncracked body generated by having recourse to the intrinsic one. One of the most popular TSL for the extrinsic approach was proposed by Camacho and Ortiz (1996) in 2D (and Pandolfi and Ortiz 1999 in 3D). There, the cohesive law is a linear decreasing function of the effective opening displacement and is derived from a free potential energy.

In this work we have used a TSL, previously reported in Snozzi and Molinari (2012), which allows us to define two separate values for energy dissipation in mode I and II ($G_{c,I}$ and $G_{c,II}$). The cohesive law resorts to the classical model of Camacho and Ortiz. Nevertheless, conversely to the Camacho Ortiz TSL, the cohesive tractions are not anymore bounded by a free potential energy (as previously suggested in Von den Bosch et al. (2005) for the intrinsic cohesive model of Xu and Needleman 1993). The tractions are assumed to be a function of an effective scalar displacement, which has the following form:

$$\delta = \sqrt{\frac{\beta^2}{\kappa^2}\,\Delta_t^2 + \Delta_n^2} \tag{3}$$

where Δ_n and Δ_t represent the normal and the tangential separation over the cohesive surface with unit outward normal $\mathbf{n}$ and unit tangential vector $\mathbf{t}$ respectively. The parameter β accounts for the coupling between normal and tangential displacement, whereas κ enables us to define the ratio between the dissipated fracture energy in mode II ($G_{c,II}$) and in mode I ($G_{c,I}$)

$$\kappa = \frac{G_{c,II}}{G_{c,I}} \tag{4}$$

In case of crack opening the traction vector is defined as follows:

$$\mathbf{T} = \left(\frac{\beta^2}{\kappa}\Delta_t\mathbf{t} + \Delta_n\mathbf{n}\right)\frac{\sigma_c}{\delta}\left(1 - \frac{\delta}{\delta_c}\right) \quad \text{for} \quad \delta = \delta_{max} \tag{5}$$

where σ_c represents the local material strength and δ_c denotes the effective relative displacement beyond which complete decohesion occurs, while δ_{max} stores the maximal effective opening displacement attained and enables thus to account for the irreversibility of the law (similarly to Camacho and Ortiz 1996). Unloading or reloading occurs if $\delta < \delta_{max}$, which results in the following tractions:

$$\mathbf{T} = \left(\frac{\beta^2}{\kappa}\Delta_t\mathbf{t} + \Delta_n\mathbf{n}\right)\frac{\sigma_c}{\delta_{max}} \times \left(1 - \frac{\delta_{max}}{\delta_c}\right) \quad \text{for} \quad \delta < \delta_{max} \tag{6}$$

2.2 Contact enforcement

Since the failure process of concrete can involve, besides cracking, frictional contact between the cracked rough surfaces, one has to enforce the impenetrability condition. For this purpose it is possible to simply avoid contact by adding a penalty term in case of negative normal opening ($\Delta_n < 0$ in the TSL). However, because our goal is to be able to deal with numerous asperities entering into contact and large displacements, we have preferred to couple the TSL with a contact algorithm. Since our numerical setup is implemented in an explicit dynamic code, we have selected an explicit master-slave contact algorithm called decomposition contact response (DCR) developed by Cirak and West (2005). This method resorts to the conservation of linear and

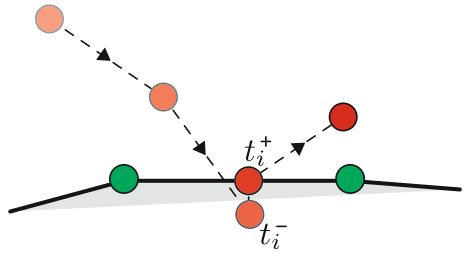

Fig. 1 Penetration removed by projecting back penetrating node on the master surface

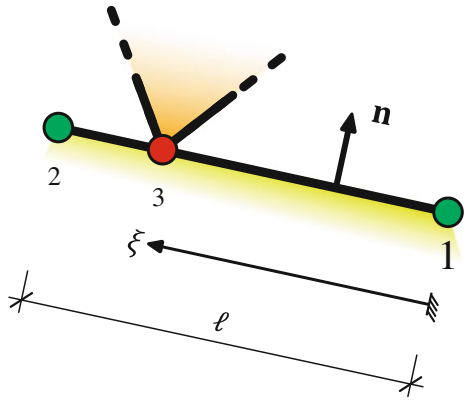

Fig. 2 Contacting triplet: node 1 and 2 belong to the target edge, whereas node 3 is the impacting node

angular momentum, while the impenetrability condition is enforced directly on the displacements, e.g. by projecting the impacting slave nodes on the penetrated master surface (Fig. 1).

The quantity of motion of the contacting nodes after collision is governed by the following equations

$$\mathbf{p}^{t_i^+} - \mathbf{p}^{t_i^-} = \lambda \nabla_{\mathbf{x}} g(\mathbf{x}^{t_i^+}) \tag{7}$$

$$\left[\mathbf{p}^T \mathbf{M}^{-1} \mathbf{p}\right]_{t_i^-}^{t_i^+} = 0 \tag{8}$$

where $\mathbf{p} = \mathbf{M}\dot{\mathbf{x}}$ represents the momentum vector of slave and master nodes ($\mathbf{x}$ position vector), g is the gap function, λ a scalar parameter and t_i^- and t_i^+ refer to the stage before and after projection within the same time step. The impact between a master surface (edge) and a slave node is schematically illustrated in Fig. 2. As illustrated in the figure, the node 3 has been already projected onto the surface, the gap function is thus equal to the distance between node 1 and node 3 projected on the segment direction, which can be expressed as follows:

$$g = \mathbf{n}^T (\mathbf{x}_3 - \mathbf{x}_1) \tag{9}$$

Once the gap function has been determined the post-impact velocities of the contacting nodes need to be corrected according to Eqs. 7 and 8.

$$\dot{\mathbf{x}}^+ = \dot{\mathbf{x}}^- - \dot{\mathbf{x}}_n^-(1 + c_{res}) - \dot{\mathbf{x}}_{fric}^- \tag{10}$$

where c_{res} represents the coefficient of restitution, which can range between zero (completely inelastic contact) and one (perfectly elastic contact) and the superscripts $^+$ and $^-$ denote quantities before and after projection respectively. For the remainder of the paper we will keep c_{res} equal to zero. Two terms need therefore to be computed: $\dot{\mathbf{x}}_{fric}$, which accounts for friction, and $\dot{\mathbf{x}}_n$, which represents the normal quantity of motion exchanged during impact. The latter is defined by

$$\dot{\mathbf{x}}_n = \left(\frac{(\nabla g)^T \dot{\mathbf{x}}}{(\nabla g)^T \mathbf{M}^{-1} \nabla g}\right) \mathbf{M}^{-1} \nabla g \tag{11}$$

In order to account for friction the relative motion between the contacting triplets (two master nodes and one slave node) needs to be corrected according to a simple Coulomb friction law which accounts for stick/slip. To this end one needs to extract the velocity leading to relative tangential separation. First the slide components of the velocity can be computed:

$$\dot{\mathbf{x}}_{slide} = \mathbf{M}^{-1} (\nabla \mathbf{h})^T \left(\frac{(\nabla \mathbf{h})\dot{\mathbf{x}}}{(\nabla \mathbf{h})\mathbf{M}^{-1}(\nabla \mathbf{h})^T}\right) - \dot{\mathbf{x}}_n \tag{12}$$

where $\mathbf{h}$ stands for the separation vector between impacting node and target segment. This can be expressed as

$$\mathbf{h} = \mathbf{x}_1 \xi + \mathbf{x}_2 (1 - \xi) - \mathbf{x}_3 \tag{13}$$

where the parameter $\xi \in [0, 1]$ stands for the relative location on the edge at which impact occurs as illustrated in Fig. 2. $\dot{\mathbf{x}}_{slide}$ represents therefore the velocity leading to a tangential relative motion between the bodies and corresponds to the maximal impulse which can be delivered during friction (i.e. stick case). Whereas, in case of slip, according to Coulomb's friction law, the correction depends on the coefficient of friction μ and on the amount of exchanged motion during impact $\dot{\mathbf{x}}_n$.

$$\dot{\mathbf{x}}_\mu = \mu \frac{\|\dot{\mathbf{x}}_n^T \mathbf{M}^{-1} \dot{\mathbf{x}}_n\|}{\|\dot{\mathbf{x}}_{slide}^T \mathbf{M}^{-1} \dot{\mathbf{x}}_{slide}\|} \dot{\mathbf{x}}_{slide} \tag{14}$$

Thus, the delivered frictional impulse will be equal to the smallest value between the slip (14) and stick (12) velocity:

$$\dot{\mathbf{x}}_{fric} = \min\left(\dot{\mathbf{x}}_{slide}, \dot{\mathbf{x}}_\mu\right) \tag{15}$$

2.3 Coupling

Mixed mode crack propagation implies that some micro-cracks might grow and debond without the generated surfaces entering into contact before the crack is fully debonded. On the contrary, other interfaces might already experience contact during this phase. Therefore, it is important to define how friction and decohesion act on the same surface during this process. In the proposed approach the TSL and the contact algorithm are coupled together in parallel.

This implies a simultaneous onset of fracture and friction if a crack is growing under compression. However, we consider a progressive rise in the amount of frictional force during debonding. I.e. when the cohesive zone is activated, friction does not act on the inter-element boundary, but it increases gradually with progressive damage of the cohesive zone following the relation:

$$1 - \left(1 - \frac{\delta}{\delta_c}\right)^q \tag{16}$$

where the exponent q has been set in this work to three. This results in a continuous progressive transition from debonding to the pure frictional stage. During this shift (when Δ_t reaches $\kappa\delta_c/\beta$) a fracture energy corresponding to $G_{c,II}$ multiplied by the length of the cohesive zone will have been dissipated. This approach produces a strength failure envelope for concrete drawn in Fig. 3b. The parameters (σ_c, δ_c, μ, κ and β) of the interfacial zone need to be identified according to the chosen material as reported in Sect. 3.

3 Meso-scale model of concrete

Concrete is a heterogeneous brittle material made of various components, which are present in different proportions. This produces a quasi-brittle material, whose mechanical behavior is defined by the wide range of the ingredients in the mixture. Considering concrete at a meso-scale level of observation allows to describe it as a biphasic material: aggregates embedded in a mortar paste matrix. In our model only medium and large aggregates are represented explicitly. Whereas, small aggregates and other components are assumed to be mixed up with the cement paste establishing the matrix phase. Besides those two components, the interfaces between the two constituents, called interfacial transition zone, are represented by dynamically inserted elements with the presented cohesive-frictional capability.

3.1 Mesh generation and aggregate distribution

The specimen geometry has been obtained using a pseudo-random generator of irregular polygons. The polygons, which represent aggregates, are created according to a chosen specific distribution. According to this, the approximate total number of inclusions can be first determine before the geometry is generated. The boundaries of each aggregate are then created by generating its faces; a random length is assigned to every edge (as well as an arbitrary angle with the previous edge). However, these values have to lie between given threshold values. Consequently, small inclusions are more likely to get fewer edges, while bigger ones show

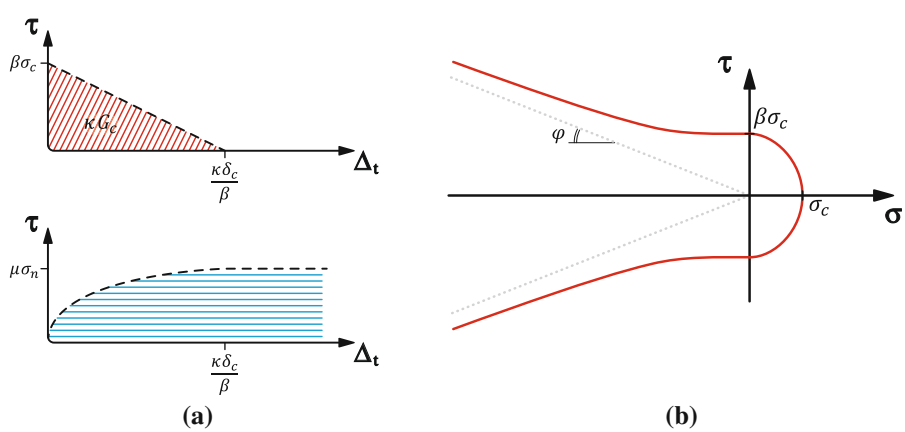

Fig. 3 **a** Shear stress-tangential opening displacement relationship for a growing crack in mode II and **b** strength failure envelope: maximal strength of inter-element faces (continuous *red line*) and residual strength after complete debonding (*gray dotted line*)

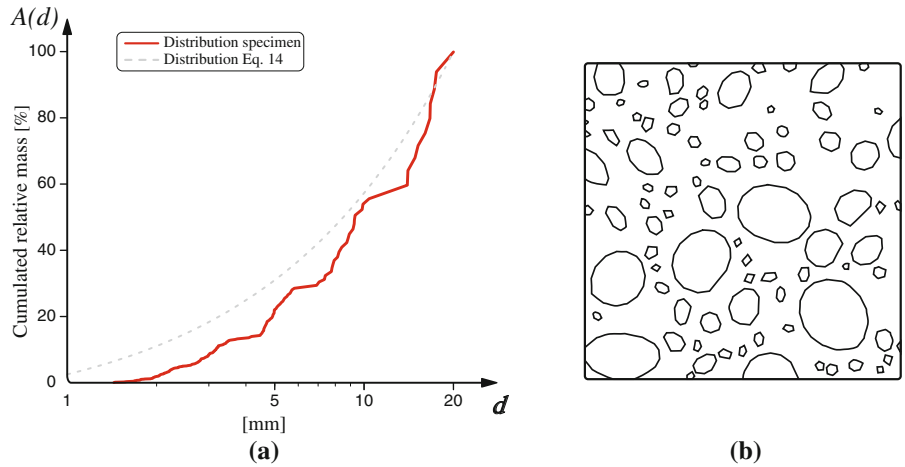

Fig. 4 **a** Computed cumulated aggregates size distribution of the concrete meso-structure (**b**)

more faces. Finally, the polygons can be placed randomly into the sample starting from the biggest ones and avoiding possible intersections with the already existent inclusions by changing location and rotating them. Although, in order to have a regular distribution of the phases near the boundaries, the aggregates have been placed in a larger area, from which the specimen has been cut out. Inclusions with the smallest diameter ranging from 1.5 to 20 mm have been considered in this work. The distribution has been chosen according to the Fuller and Fuller and Thompson (1907) curve with a value for the exponent q equal to 0.7.

$$A(d) = \left(\frac{d}{d_{max}}\right)^{q} \tag{17}$$

Where A(d) represents the percent by weight (cumulated mass under a given diameter d) and d_{max} the largest aggregate in the mixture. This idealized curve is plotted in Fig. 4a together with the recorded distribution within the sample having the generated meso-structure of Figure 4b. The obtained distribution differs from the reference one of Eq. 17 in its starting value (since inclusions smaller than 1.5 mm have been not represented explicitly) and in the discontinuous shape (small specimen size and discrete inclusions).

The resulting ratio of aggregate area is around 31 % of the specimen area, which is a square with an edge size equal to 100 mm. For the remainder of the paper we have kept the same geometry for every simulation. Indeed, a different meso-structure with a similar distribution would not affect significantly the results as reported in Gatuingt et al. for tensile loading (since the specimen dimension can be considered large enough). From this geometry one can obtain meshes with different element sizes. Since a convergence study on mesh sensitivity has already been performed in previous work (Snozzi et al. 2011; Gatuingt et al.), we have set directly the value of the average element size to 0.5 mm (which gives a mesh with roughly 120,000 nodes).

3.2 Material parameters

The meso-mechanical approach requires defining the material properties for every component. In Table 1 the material properties for the inclusions and matrix paste are summarized. Those values are generic and suitable for a usual concrete and reflect the values used (by the authors) in previous work Snozzi et al. (2011).

The values for the three different interfaces are reported in Table 2. These material properties can be determined experimentally (for instance Rosselló et al. 2006). For this work we have chosen values of the cohesive properties (G_c and σ_c) similar to the ones reported in Gatuingt et al. while the remaining pair (β, κ) had to be identified through a parametric study as reported in Sect. 4.

Table 1 Material properties of the concrete's components

Material	Density—ρ [kg/m^3]	Young's modulus—E [GPa]	Poisson's ratio—ν [−]
Aggregate	2, 700	75	0.2
Cement paste	2, 200	30	0.2

Table 2 Cohesive properties and selected parameters for the interfaces

Interface	Fracture energy G_c— [J/m^2]	Tensile strength σ_c— [MPa]	β	κ	Friction coefficient μ—[−]
Aggregate	60	16	3.5	10	0.7
Mortar paste	50	4.7	3.5	10	0.7
ITZ	30	2.7	3.5	10	0.7

4 Uniaxial tensile/compressive loading

In this section we analyze the dynamic tensile and compressive response of the concrete model.

4.1 Initial and boundary conditions

The samples are loaded under displacement control with an imposed strain rate $\dot{\varepsilon}$. For tension all the nodes of the finite element mesh which are located on the upper (respectively lower) boundary are forced to move at a constant velocity $V_{0y} = V_0$ (respectively $V_{0y} = -V_0$) as illustrated in Fig. 5a):

$$V_0 = \dot{\varepsilon}\frac{h}{2} \tag{18}$$

where h is the height of the studied specimen. To avoid important stress wave propagation and an early fracture near the boundaries Miller et al. (1999), all nodes of the finite-element mesh are prescribed an initial velocity as illustrated in Fig. 5a:

$$V_y(y) = \frac{2V_0}{h}y \tag{19}$$

Note that, even if the linear gradient is not exact in case of a heterogeneous material, the selected initial condition does not lead to oscillations at early stage of loading. In case of compression (Fig. 5b) nodes located at the upper edge of the finite element mesh are forced to move at a certain constant velocity V_0:

$$V_0 = -\dot{\varepsilon}h \tag{20}$$

whereas, the lower boundary is supported in y-direction and therefore the motion of the nodes belonging to this edge is blocked in the vertical direction (while the horizontal displacement of the nodes is unconstrained). If lateral confinement (p_x) is applied (Sect. 5), the sample is first loaded statically with a hydrostatic pressure

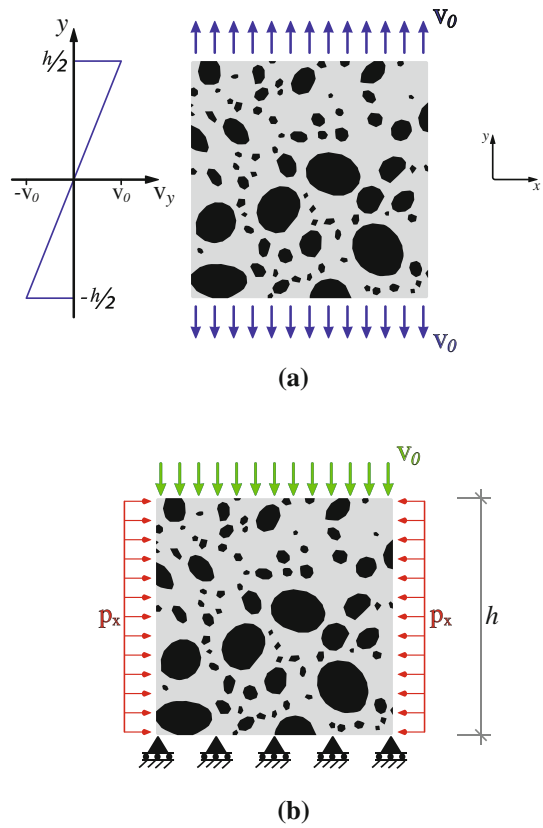

Fig. 5 Boundary and initial conditions for specimen loaded in **a** tension and **b** compression

corresponding to p_x. After this step, the dynamic loading is applied until the end of the simulation.

To obtain the stress-strain curves presented thereafter, we define the macroscopic stress (σ) as the boundary reaction force F_y divided by the initial width, and the macroscopic strain (ϵ) as the change in height divided by the initial height h. In case of compression, the compressive stress and compressive strain are identified with σ_c and ϵ_c respectively. Moreover, during simulation, a slight material damping has been adopted in order to compensate the slight increase of internal energy (due to the enforcement of the impenetrability through projection Cirak and West 2005) and reduce numerical oscillations.

4.2 Identification of model's interface parameters through simulations

In order to identify the two remaining parameters of the cohesive law, β and κ, we have ran some simulations in

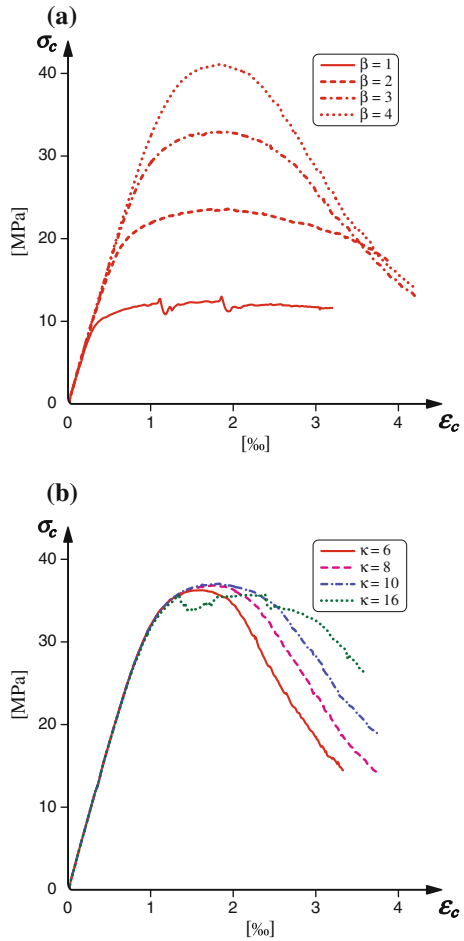

Fig. 6 **a** Influence of the β parameter on the compressive stress-strain behavior of concrete (for $\kappa = 10$) and **b** influence of κ (with $\beta = 3.5$) for $\dot{\varepsilon} = 1\, s^{-1}$

order to extract them indirectly by comparing the macroscopic stress-strain relationship with a semi-empirical model for concrete proposed by Fernández Ruiz et al. (2007) for the compressive behavior.

Since these two parameters influence mode II cracking, and have therefore little influence on the peak tensile strength and more generally on the global macroscopic behavior of the specimens subjected to uniaxial tension, the fitting has been conducted by examining the response in unconfined compression for a loading rate $\dot{\varepsilon} = 1\, s^{-1}$. The influence of β has been investigated first. Its value affects the shear strength of the interfaces, which changes considerably the compressive peak strength of concrete as depicted in Fig. 6a. With an increasing value of β, one obtains a higher compressive strength. Since with the interface properties of Table 2 a tensile strength slightly lower than 4 MPa (precisely 3.67 MPa) is obtained, the authors have decided to set the value of β equal to 3.5 (a lower value compared to the one chosen in Ruiz et al. 2000). This leads to a compressive strength roughly one order of magnitude higher than the tensile one (see Fig. 7b), which seems a usual ratio for a conventional concrete. The stress-strain behavior is also affected by κ, which increases the dissipated fracture energy and therefore modifies mostly the post-peak behavior and shifts the transition to softening towards higher strain values. This trend is graphically illustrated in Fig. 6b. Therefore, in order to obtain a concrete with softening starting around $\epsilon_c = 0.002$ (which is a usual value for the peak strain of conventional unconfined concrete) we decided to fix the value of κ at 10 (same ratio between fracture energies estimated by Carol et al. 2001). Note that this relatively high value should take into account frictional effects that might occur for low normal openings of the surfaces that are not taken into account by the frictional contact algorithm. This results in a concrete with a compressive strength of roughly 36.8 MPa at a compressive peak strain around 0.0019. The obtained constitutive response is compared in Fig. 7a with the constitutive model proposed in Fernández Ruiz et al. (2007). The computed peak strain and stress are in the same range of the experimental values ($\epsilon_{peak} = 0.0018 - 0.0021$ and $\sigma_{peak} = 32.8 - 38.8$) recorded by Sfer et al. (2002). Note that we could not compare directly the curves since the experimental unconfined response is not drawn in Sfer et al. (2002). Nevertheless, we will have recourse again to the data reported in this reference for the comparison with the confined response in compression (Sect. 5). The stress-strain behavior is depicted for tension and compression in Fig. 7b. It is clear that the tension/compression asymmetry is well captured.

4.3 Rate effect

In this subsection we analyze the behavior of concrete subjected to tension and unconfined compression under different loading rates.

4.3.1 Tensile response

It is well-known that experimental results on dynamic tension tests show a rate sensitivity of the tensile

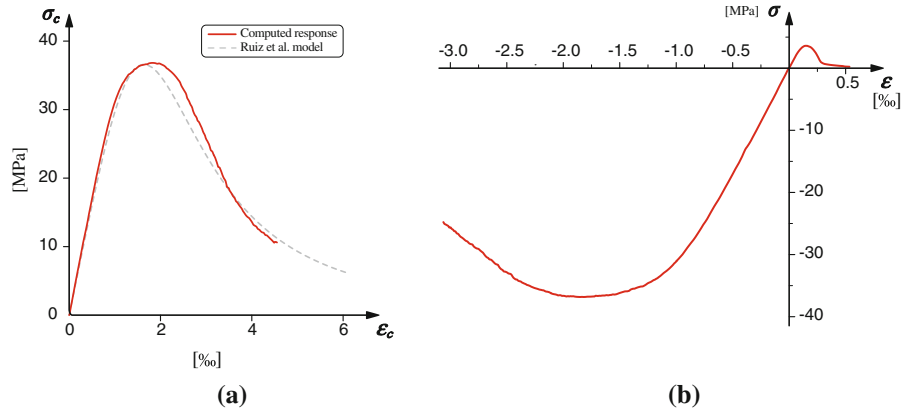

Fig. 7 **a** comparison with empirical model of Fernández Ruiz et al. (2007) and **b** asymmetric tensile/compressive behavior of concrete ($\dot{\varepsilon} = 1\,s^{-1}$)

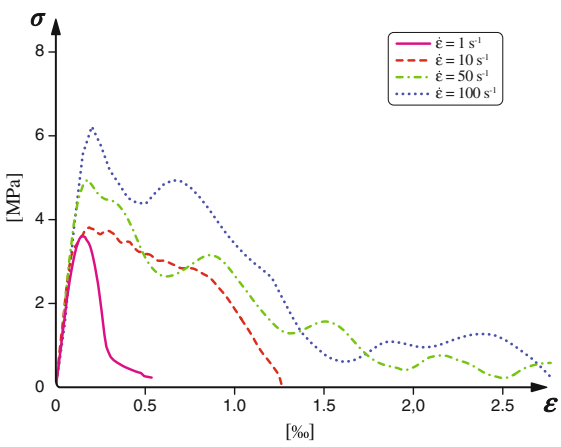

Fig. 8 Influence of strain rate on the tensile stress-strain curves

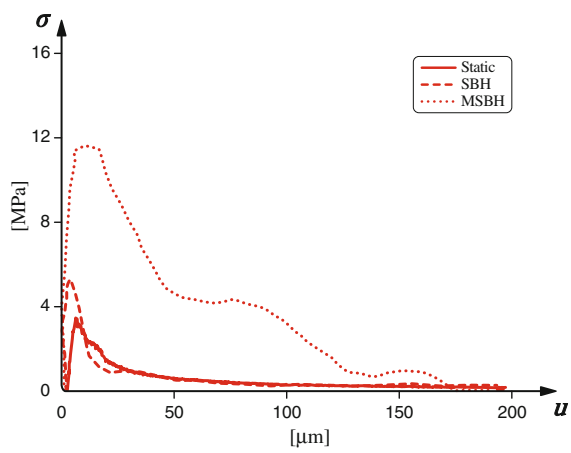

Fig. 9 Experimental stress-displacement curves for static, SHB and Modified SHB reported in Weerheijm et al. (2009)

strength (Vegt et al. 2006; Erzar and Forquin 2010). In quasi-statics, the macroscopic tensile strength is mainly governed in our case by the ITZ strength and toughness (ITZ between the aggregates and the mortar paste) and not by the meso-structure (Pedersen et al. 2007; Gatuingt et al.). For low strain rates—$\dot{\varepsilon} < 1$ /s—the dynamic resistance increase is mainly due to the presence of water in the material Rossi et al. (1992) and we have a slight Dynamic Increase Factor (DIF)—equal to the ratio of static versus dynamic strengths. For higher strain rates—$\dot{\varepsilon} > 1$/s—the usual explanation of a more important DIF is the transition between single cracking in quasi-statics to diffuse cracks in dynamics.

The results of the strain-stress curves obtained for our numerical simulations in tension for several strain rates are presented in Fig. 8. As expected, the transition from a unique crack to diffuse cracking has a strong influence on the macroscopic behavior of concrete. Increasing the strain rate delays (relatively) the coalescence of the microcracks, which rises the peak strength. One can notice that oscillations appear in the response of the sample during the softening stage when an increasing strain rate is applied. Experimental recorded curves, as for instance those illustrated in Fig. 9, show a similar shape. Note that data on experimental tests of Split Hopkinson Bar (as the one depicted in Fig. 9) express concrete behavior in terms of force-displacement relationship (and to convert them in stress-strain relationship is not an evident task). We can notice that in our case the dynamic increase factor is equal to almost 2 for $\dot{\varepsilon} = 100$/s which underestimates a little bit the experimentally reported values (~ 3 Weerheijm et al. 2007). This implies that we may have to take into account rate dependency at the material level, for example by linking the cohesive strength σ_c to the rate of deformation of the surrounding material

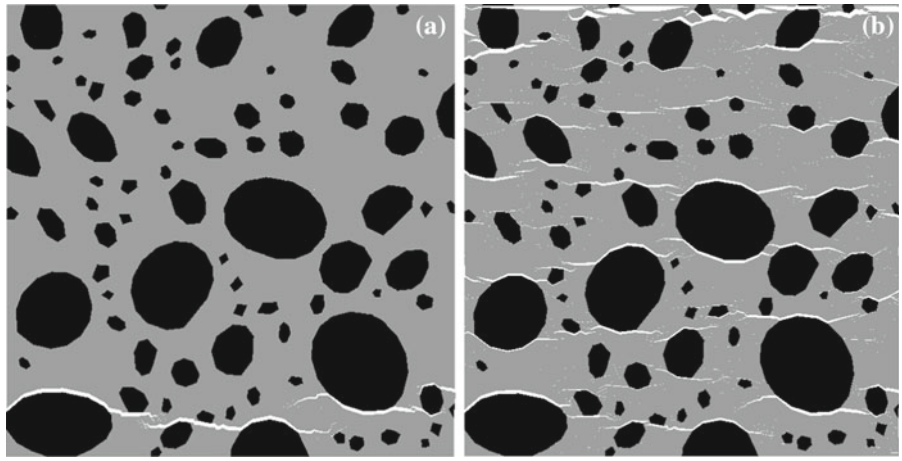

Fig. 10 Influence of strain rate on the crack path in uniaxial tension: **a** $\dot{\varepsilon} = 1\,s^{-1}$, **b** $\dot{\varepsilon} = 100\,s^{-1}$. Displacement has been magnified by a factor of 20

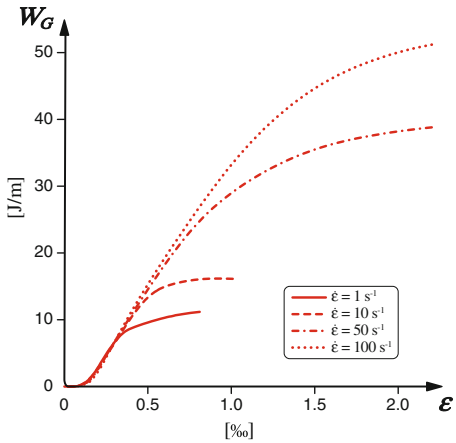

Fig. 11 Influence of strain rate on the dissipated energy for tensile loading

and to the crack opening rate, in order to achieve better agreement with experimental results. We may nonetheless conclude that the dynamic increase factor is mostly due to a "structural effect", with probably a small part due to a viscous behavior of the matrix paste. Figure 10 shows the final crack patterns for a low and a high strain rate. For $\dot{\varepsilon} = 1/\mathrm{s}$ we have a unique macroscopic crack, while for $\dot{\varepsilon} = 100/\mathrm{s}$ we obtain diffuse cracks. In both cases, microcracks, for the most part, succeed to find paths around the aggregates.

Figure 11 depicts the evolution of the dissipated fracture energy as a function of the macroscopic strain of the specimen for different loading rates. One can remark from this figure that the dissipated fracture energy strongly depends on the loading rate even with a rate independent local fracture energy. Nevertheless as for the strength, the DIF for the dissipated fracture energy (W_G) in the specimen is slightly lower than the experimental one Weerheijm et al. (2007). For more detail on the tensile response of our model, one can refer to Gatuingt et al.

4.3.2 compressive response

As for tension, experimental results (Bischoff and Perry 1991) show a clear rate sensitivity under compressive loading. Commonly, the stress increase can be explained with lateral inertial confinement (Poisson's effect) and a more diffuse micro-cracking beside eventual material rate hardening mechanisms.

Figure 12 shows the computed stress-strain curve for different loading rates. The results display a strain rate hardening with a DIF of about 1.9 for a strain

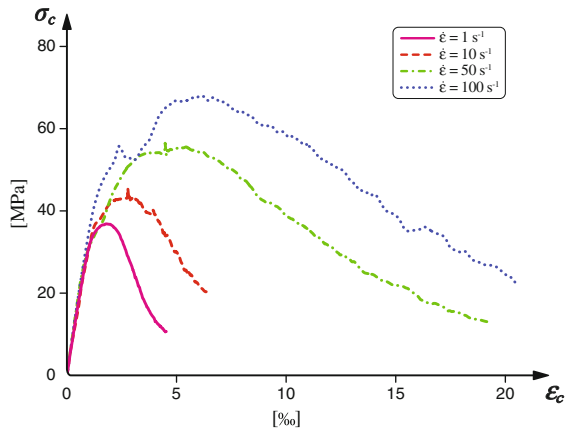

Fig. 12 Stress-strain response for different strain rates under compressive loading

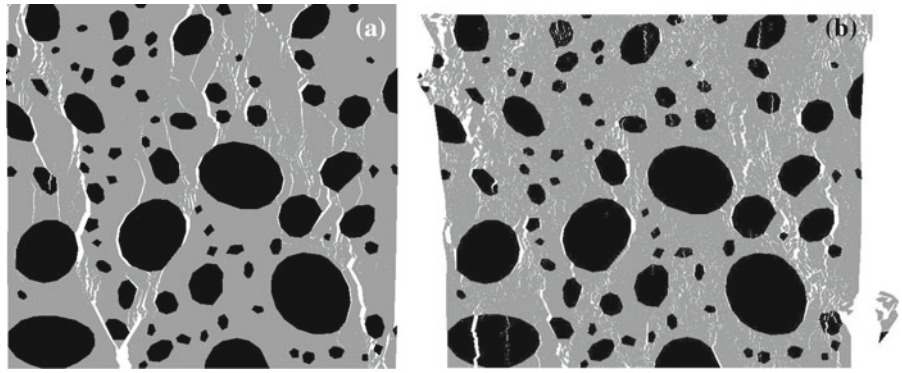

Fig. 13 Influence of strain rate on the crack path in compression: **a** $\dot{\varepsilon} = 1\ s^{-1}$, **b** $\dot{\varepsilon} = 100\ s^{-1}$. Note that the displacement field has been magnified by two different factors: 4 in (**a**) and 2 (**b**)

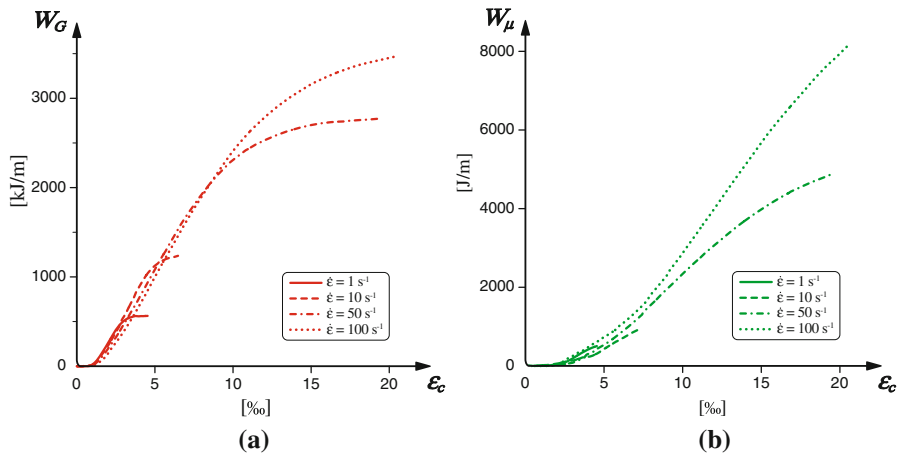

Fig. 14 **a** Dissipated fracture energy and **b** dissipated frictional work for different loading rates

rate of $\dot{\varepsilon} = 100\ s^{-1}$. In contrast to our computed tensile DIF, this increase factor is consistent with experimental results Bischoff and Perry (1991). This results highlights the strong effect of lateral inertial confinement alone that can explain the increase in strength as noticed in Donzé et al. (1999) too. Indeed, in our simulations, we do not consider any rate effect at the material level. Figure 13 shows the crack pattern for $\dot{\varepsilon} = 1\ s^{-1}$ and $100\ s^{-1}$. Cracks tend to propagate within the matrix phase bypassing the inclusions except for few big aggregates that have been crossed. One can notice that due to the absence of a horizontal constraint at the upper and lower boundaries of the specimen, the crack pattern does not show the formation of a characteristic cone, as mostly observed during simple compression experiments. Moreover, the cracks are aligned parallel to the loading direction, conversely to a perpendicular orientation in case of tension as shown in Fig. 10.

The evolution of the dissipated fracture energy (W_G) and frictional work (W_μ) in the specimen is depicted in Fig. 14a, b respectively. Both figures show that the raising number of cracks with increasing strain rate causes a higher dissipation of energy within the damaged specimen. This mechanism leads to a higher compressive strength and larger area (thus toughness) under the stress-strain curve. In particular, the post-peak dissipation of energy seems to be affected more by friction than by dissipation of fracture energy. Therefore, the gain in strength can be traced back to an inertial effect alone (as suggested for instance in Cotsovos and Pavlović 2008).

5 Influence of lateral confinement

We now investigate the behavior of concrete subjected to moderate lateral confinement under a strain rate $\dot{\varepsilon} = 1\ s^{-1}$. The concrete specimens have been subjected to four level of transversal confinement pressures (p_x): 4.5, 9, 12 and 30 MPa (for comparison with experiments).

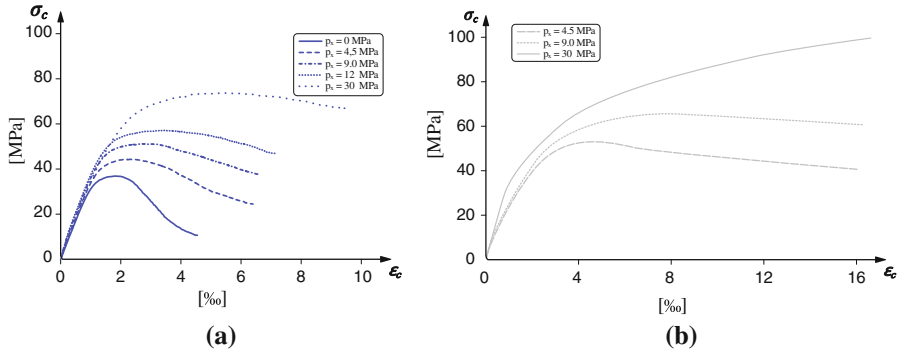

Fig. 15 **a** Influence of confining pressure on the stress-strain behavior ($\dot{\varepsilon} = 1\,s^{-1}$) and **b** experimental results of Sfer et al. (2002)

Figure 15a shows that the confining stress increases substantially the compressive strength as well as the longitudinal compressive peak strain. Moreover, one can notice that confining concrete results in a decrease of the slope of the post-peak branch indicating therewith a moderate rise in the ductility of concrete. Among the several data that one can find in the experimental literature of the stress-strain behavior, we have selected the data on triaxial loading reported in Sfer et al. (2002) for a direct comparison. As previously commented the concrete tested in this reference almost matches in terms of peak strength and peak strain the computed response in the unconfined case. The comparison between simulations and the results is illustrated in Fig. 15. As already noticed, one can remark that the increase in peak strength with lateral confinement in the simulations is lower than the one obtained experimentally. Additionally, one can compute the gain in concrete strength of the confined specimens. Usually, in concrete research, the Mohr–Coulomb failure criterion can be assumed to describe the sliding failure in a confined concrete. This can be expressed as follows:

$$\sigma_c = f_c + k * p_x \tag{21}$$

where f_c represents the unconfined compressive strength of concrete and k is a constant, which is usually set to four (Richart et al. 1929; Lahlou et al. 1992; Candappa et al. 2001) for triaxial tests. In our case, we obtain a k with a value somewhat lower than two for low confining pressures (and that becomes even smaller if moderate pressures are considered), while the increase measured by Sfer et al. (2002) (Fig. 15b) gives a k of roughly 3.5. Moreover, the values recorded by Sfer et al. (2002) show a considerable raise in ductility of the specimen with larger confinement. While simulations show only a moderate increase. This becomes more evident for the highest confining pressure (30 MPa) considered here. At such confining pressures the specimen response is probably dominated by physical interactions at the micro-crack level that our model seems to reproduce less accurately. The failure mechanism shifts from damage due to strain extension to compaction due to porosity reduction. Some authors (e.g. Camborde et al. 2000) are able to reproduce compaction with a lattice based discrete element method introducing a phenomenological model in their beam behavior. Another reason for the too little hardening could partially reside in an insufficient dissipation of frictional energy in our simulations, which leads to a larger negative slope after the peak strength has been reached. A better modeling could perhaps be obtained by increasing the value of the friction coefficient and acting on the coupling (apart from changing the value of the pair β and κ). Indeed, the chosen onset of friction implies an initiation of cracks that is not influenced by the level of applied lateral pressure. In addition, it should also be pointed out that the chosen 2D framework is limited and cannot capture realistic 3D micro-cracking networks. Indeed in three dimensions to reach percolation is more difficult than in 2D, where cracks can coalesce easily. This implies that in 2D the obtained micro-cracks density might be underestimated and consequently the dissipation of energy as well. This work can be considered as a first attempt to extract concrete behavior from a new approach and the foreseen improvement clearly requires an extension to 3D.

The comparison between the dissipated energies is illustrated in Fig. 16. From Fig. 16a one can remark that an increase in the lateral confinement will delay the opening of cracks and thereafter the start of the dissipation of fracture energy. This phenomenon has already been observed with a meso-scale modeling of ceramics (Warner and Molinari 2006; Kraft et al. 2008). However, the rise in the horizontal pressure ultimately

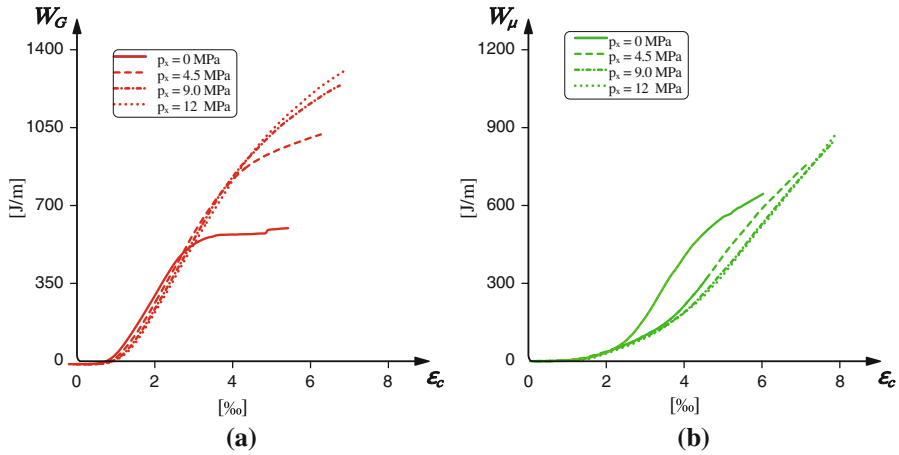

Fig. 16 **a** Dissipated fracture energy and **b** frictional work for $p_x = 0, 4.5, 9$and12 MPa ($\dot{\varepsilon} = 1\, s^{-1}$)

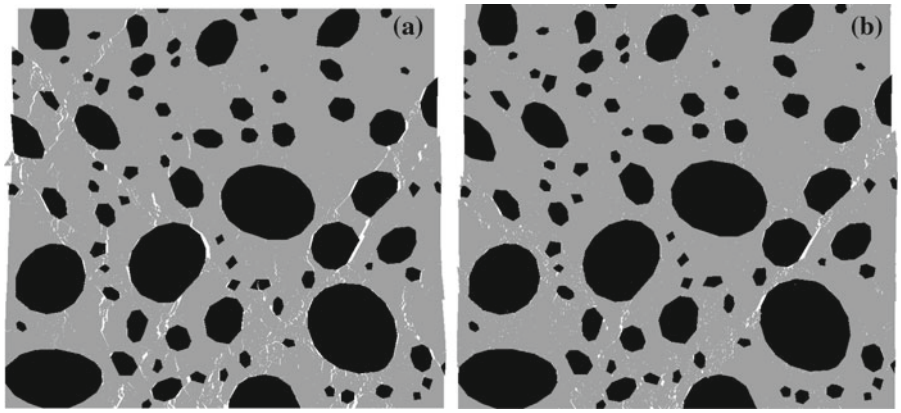

Fig. 17 Deformed specimens for confinement pressures of **a** 4,5 Mpa and **b** 12 MPa. Displacement has been magnified by a factor of 5

increases the amount of dissipated fracture energy. This is because cracks are more prone to open following a mode II fashion, which is bounded with a larger value of stored fracture energy than mode I, and also because there is a more diffuse fine crack network. Figure 17 shows this crack network. It also illustrates that applying a confinement pressure forces the cracks to propagate at a faulting angle of roughly 30°, whereas their paths were more vertical for unconstrained compression (Fig. 13a). The increase in the faulting angle orientation, from axial splitting for unconfined concrete to shear faulting for specimens subjected to lateral confinement, appears to be in agreement with analytical models (see for instance Horii and Nemat-Nasser 1985 for rock mechanics).

Since we are using an explicit representation of cracks, it is possible to monitor their time evolution and to extract relevant information. We have chosen to follow the formation of the longest crack cluster (which is a group of fully broken interfaces which are interconnected to each other), $L_{c,max}$, as well as the total number of crack clusters NB_c (as was done for ceramics in Warner and Molinari 2006; Kraft et al. 2008). The first variable has been normalized with the edge size of the specimen. As already observed, an increase in the level of confinement produces a delay in the formation of the first cluster. This is noticeable from both graphs of Fig. 18. Moreover, from the first graph (Fig. 18a) one can see that the application of a horizontal pressure causes the longest crack to be relatively shorter with a length of the range of $0.2h$ (unfolded length) until the negative slope of the softening becomes more pronounced. On the other hand, the number of clusters is not much affected by the application of lateral confinement as depicted in Fig. 18b. The unconfined sample shows initially a larger number of cracks than the confined ones, which implies that the lateral pressure delays the onset of micro-cracks coalescence. This can be confirmed by looking at the deformed mesh configuration. One can

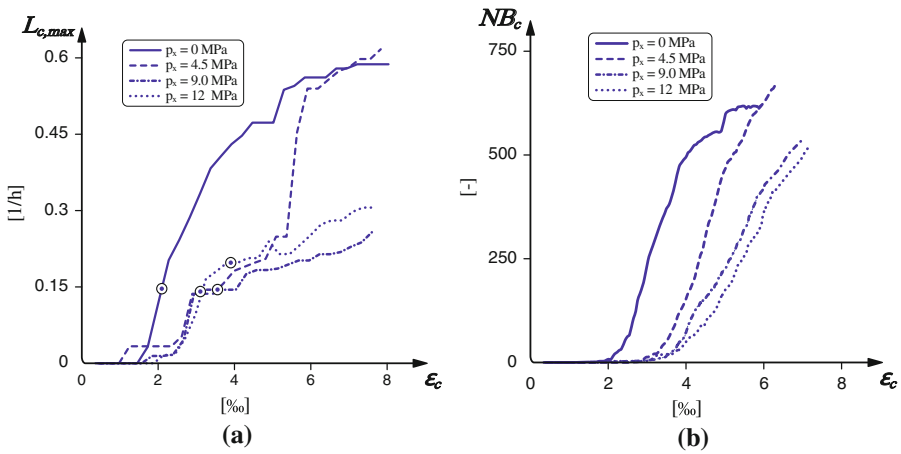

Fig. 18 **a** Maximal cluster length normalized over specimen size h and **b** number of cracks for $p_x = 0$, 4.5, 9 and 12 MPa. The length at which softening starts, represented by circles on graph (**a**), does not depend on the amount of confinement

see from Fig. 17 that the application of the confinement pressure triggers a finer net of smaller cracks, which exhibit a smaller opening (and are thus not completely debonded). Finally, by looking at Fig. 18a, it appears that the softening phase can start, for the three confined cases considered here, when the longest cluster reaches a length of approximately 0.15–0.2 h (circles on the strain-$L_{c,max}$ curve indicate the strain immediately after peak strength has been reached) and thus does not depend on the level of applied confinement (For the unconfined sample the transition is less clear to identify, since the transition to a macroscopic crack is more rapid). Note that the total length of a cluster has been considered here, whereas if one looks at the cluster length projected on a line (similarly to what reported in Prado and van Mier (2003) for tensile loading), its maximal value will not increase much after the softening has started. That is, the maximal projected length tends to stabilize around 0.2–0.15 h.

6 Discussion and conclusions

In this paper we have presented a 2D dynamical meso-mechanical model of concrete with cohesive/frictional capability for transient dynamics. The meso-scale approach enables us to represent aggregates and mortar explicitly, thus allowing all material parameters to be physically identified. Both continuum phases are considered to behave elastically while initiation, coalescence and propagation of cracks are modeled by dynamically inserted interface elements with the proposed cohesive frictional capability. The debonding process is controlled by an extrinsic TSL which accounts for path dependent behavior and therefore enables us to define two separate values for energy dissipation in mode I and II. The impenetrability condition is enforced directly by projecting the impacting nodes on the penetrated surface.

We have used this model to simulate dynamic concrete's behavior in traction and compression. From the obtained results we can draw the following conclusions.

Simulations in tension as well as in compression show that the model gives an increase in peak strength and strain at failure with increasing rate of loading although the interfacial constitutive law is rate independent. This rise in strength resides in a more diffuse micro-cracking and is thereby bounded with a higher dissipation of fracture energy as well as energy dissipated through friction in case of compressive cracking. A comparison between our simulation results and experimental literature indicates that inertial forces alone in case of compressive loading are sufficient to explain the increase in strength with increasing loading rate. On the contrary, if the specimen is subjected to tensile loading, a small strain-rate dependence at the material level (material hardening) should be added in order to achieve a better agreement with experimental results.

Specimens subjected to lateral confinement in compression exhibit an increase in peak strength and strain at maximum stress with increasing confining pressure. However, the rise in strength is lower than experimental reported values. It has been observed that an increase in the lateral pressure produces delays in the formation of the first crack cluster and in micro-cracks coalescence. Dissipation of energy through fracture and friction is

also an increasing function of the applied confinement. The model also shows the importance of capturing frictional mechanisms, which appear to dissipate a raising amount of frictional energy with increasing strain and applied pressure (the work done by friction is on the same range of magnitude as the energy dissipated trough crack opening under compressive loading).

It is however important to emphasize that our model needs further improvement to capture experiments better. In particular, the ductility of the specimen is less affected by the confining pressure than the one measured experimentally and the post-peak behavior remains more brittle. This could perhaps be traced back to a yet insufficient increase in the amount of dissipated frictional energy or to the lack of others physical phenomenon in the model (such as compaction). Moreover, the chosen 2D setting is limiting to capture the complexity of 3D micro-cracking. Indeed, in 2D the density of the cracks is underestimated since it is easier to reach percolation than in 3D. Besides this, the influence of the internal ordering of the meso-structure has not been investigated in this paper. In the future, we plan to use our model as a basis to investigate shearing resistance (including asperities interlocking) of structural components.

Acknowledgments This material is based on the work supported by the Swiss National Foundation under Grant no. 200021 122046/1.

References

Barenblatt GI (1962) The mathematical theory of equilibrium of cracks in brittle fracture. Adv Appl Mech 7:55–129

Bazant ZP, Caner FC, Adley MD, Akers SA (2000) Fracturing rate effect and creep in microplane model for dynamics. J Eng Mech ASCE 126(9):962–970

Bischoff PH, Perry SH (1991) Compressive behaviour of concrete at high strain rates. Mater Struct 24:425–450

Bolander JE Jr, Saito S (1998) Fracture analysis using spring networks with random geometry. Eng Fract Mech 61(5–6):569–591

Caballero A, López CM, Carol I (2006) 3D meso-structural analysis of concrete specimens under uniaxial tension. Comput Methods Appl Mech Eng 195(52):7182–7195

Camacho GT, Ortiz M (1996) Computational modelling of impact damage in brittle materials. Int J Solids Struct 33(20–22):2899–2938

Camborde F, Donzé FV, Mariotti C (2000) Numerical study of rock and concrete behaviour by discrete element modelling. Comput Geotech 27:225–247

Candappa DC, Sanjayan JG, Setunge S (2001) Complete triaxial stress-strain curves of high-strength concrete. J Mater Civil Eng 13(3):209–215

Carol I, López CM, Roa O (2001) Micromechanical analysis of quasi-brittle materials using fracture-based interface elements. Int J Numer Methods Eng 52(1–2):193–215

Cervenka J, Chandra Kishen JM, Saouma VE (1998) Mixed mode fracture of cementitious bimaterial interfaces; part ii: numerical simulation. Eng Fract Mech 60(1):95–107

Cirak F, West M (2005) Decomposition contact response (DCR) for explicit finite element dynamics. Int J Numer Methods Eng 64:1078–1110

Cotsovos DM, Pavlović MN (2008) Numerical investigation of concrete subjected to compressive impact loading. Part 1: A fundamental explanation for the apparent strength gain at high loading rates. Comput Struct 86:145–163

Cusatis G (2011) Strain-rate effects on concrete behavior. Int J Impact Eng 38(4):162–170

Desmorat R, Chambart M, Gatuingt F, Guilbaud D (2010) Delay-active damage versus non-local enhancement for anisotropic damage dynamics computations with alternated loading. Eng Fract Mech 77(12):2294–2315

Desmorat R, Gatuingt F, Ragueneau F (2010) Nonstandard Thermodynamics Framework for Robust Computations with Induced Anisotropic Damage. Int J Damage Mech 19(1):53–73

Donzé FV, Magnier S, Daudeville L, Mariotti C, Davenne L (1999) Numerical study of compressive behavior of concrete at high strain rates. J Eng Mech 125(10):1154–1162

Dubé JF, Pijaudier-Cabot G, La Borderie C (1996) Rate dependent damage model for concrete in dynamics. J Eng Mech ASCE 122(10):939–947

Dugdale DS (1960) Yielding of steel sheets containing slits. J Mech Phys Solids 8:100–108

Erzar B, Forquin P (2010) An experimental method to determine the tensile strength of concrete at high rates of strain. Exp Mech 50(7):941–955

Fernández Ruiz M, Muttoni A, Gambarova P (2007) Relationship between nonlinear creep and cracking of concrete under uniaxial compression. J Adv Concr Technol 5:383–393

Fuller WB, Thompson SE (1907) The laws of proportioning concrete. J Transp Div 59

Gatuingt F, Desmorat R, Chambart M, Combescure D, Guilbaud D (2008) Anisotropic 3D delay-damage model to simulate concrete structures. Revue Européenne de Mécanique Numérique 17:740–760

Gatuingt F, Pijaudier-Cabot G (2002) Coupled damage and plasticity modeling in transient dynamic analysis of concrete. Int J Numer Anal Methods Geomech 26:1–24

Gatuingt F, Snozzi L, Molinari JF. Numerical determination of the tensile response and the dissipated fracture energy of concrete: role of the meso-structure and influence of the loading rate. Int J Numer Anal Methods Geomech (accepted)

Grassl P, Jirásek M (2010) Meso-scale approach to modelling the fracture process zone of concrete subjected to uniaxial tension. Int J Solids Struct 47(7–8):957–968

Grassl P, Rempling R (2008) A damage-plasticity interface approach to the meso-scale modelling of concrete sub-

jected to cyclic compressive loading. Eng Fract Mech 75(16):4804–4818
Horii H, Nemat-Nasser S (1985) Compression-induced microcrack growth in brittle solids: axial splitting and shear failure. J Geophys Res 90:3105–3125
Kozicki J, Tejchman J (2007) Effect of aggregate structure on fracture process in concrete using 2d lattice model. Arch Mech 59:365–384
Kraft RH, Molinari JF, Ramesh KT, Warner DH (2008) Computational micromechanics of dynamic compressive loading of a brittle polycrystalline material using a distribution of grain boundary properties. J Mech Phys Solids 56(8):2618–2641
Lahlou K, Aitcin P, Chaallal O (1992) Behaviour of high-strength concrete under confined stresses. Cem Concr Compos 14(3):185–193
López C (1999) Microstructural analysis of concrete fracture using interface elements. Application to various concretes. Ph.D. thesis, Universitat Politcnica de Catalunya, Spain
Miller O, Freund LB, Needleman A (1999) Modeling and simulation of dynamic fragmentation in brittle materials. Int J Fract 96(2):101–125
Newmark NM (1959) A method of computation for structural dynamics. J Eng Mech 85:67–94
Ottosen NS (1979) Constitutive model for short-time loading of concrete. J Eng Mech Div ASCE 105(1):127–141
Pandolfi A, Ortiz M (1999) Finite-deformation irreversible cohesive elements for three dimensional crack-propagation analysis. Int J Numer Methods Eng 74:1393–1420
Pedersen RR, Simone A, Sluys LJ (2008) An analysis of dynamic fracture in concrete with a continuum visco-elastic visco-plastic damage model. Eng Fract Mech 75:3782–3805
Pedersen RR, Simone A, Stroeven M, Sluys LJ (2007) Mesoscopic modelling of concrete under impact. In: Proceedings of 6th International conference on fracture mechanics of concrete and concrete structures—FRAMCOS VI, pp 571–578
Pontiroli C, Rouquand A, Mazars J (2010) Predicting concrete behaviour from quasi-static loading to hypervelocity impact An overview of the PRM model. Eur J Environ Civil Eng 14(6–7):703–727
Prado EP, Mier JGMvan (2003) Effect of particle structure on mode i fracture process in concrete. Eng Fract Mech 70(14):1793–1807
Richart FE, Brandtzaeg A, Brown RL (1929) Failure of plain and spirally reinforced concrete in compression. Technical Report 190, University of Illinois, Urbana
Roelfstra P, Sadouki H, Wittmann F (1985) Le béton numerique. Mater Struct RILEM 18:309–317
Rosselló C, Elices M, Guinea GV (2006) Fracture of model concrete: 2. Fracture energy and characteristic length. Cem Concr Res 36:1345–1353
Rossi P, van Mier JGM, Boulay C, Le Maou F (1992) The dynamic behaviour of concrete: influence of free water. Mater Struct 25:509–514
Ruiz G, Ortiz M, Pandolfi A (2000) Three-dimensional finite-element simulation of the dynamic Brazilian tests on concrete cylinders. Int J Numer Methods Eng 48(7):963–994
Schlangen E, van Mier JGM (1992) Simple lattice model for numerical simulation of fracture of concrete materials and structures. Mater Struct 25(9):534–542
Sercombe J, Ulm FJ, Toutlemonde F (1998) Viscous hardening plasticity for concrete in high-rate dynamics. J Eng Mech ASCE 124(9):1050–1057
Sfer D, Carol I, Gettu R, Etse G (2002) Study of the behavior of concrete under triaxial compression. J Eng Mech 128(2):156–163
Snozzi L, Caballero A, Molinari JF (2011) Influence of the meso-structure in dynamic fracture simulation of concrete under tensile loading. Cem Concr Res 41:1130–1142
Snozzi L, Molinari JF (2012) A cohesive element model for mixed mode loading with frictional contact capability. Int J Numer Methods Eng. doi:10.1002/nme.4398
Vegt I, Pedersen RR, Sluys LJ, Weerheijm J (2006) Modelling of impact behaviour of concrete—An experimental approach. In: Computational modelling of concrete structures—EURO-C 2006, pp 451–458
Von den Bosch MJ, Schreurs PJG, Geers MGD (2005) A critical evaluation of the exponential Xu and Needleman cohesive zone law for mixed mode decohesion. Eng Fract Mech 72:2247–2267
Vonk RA (1993) Micromechanical investigation of softening of concrete loaded in compression. Heron 38:5–94
Warner DH, Molinari JF (2006) Micromechanical finite element modeling of compressive fracture in confined alumina ceramic. Acta Mater 54(19):5135–5145
Weerheijm J, Vegt I, van Breugel K (2009) The rate dependency of concrete in tension - New data for wet, normal and dry conditions. In: DYMAT 2009: 9th international conference on the mechanical and physical behavior of materials under dynamic loading, vol 1. pp 95–101
Weerheijm J, Vegt I, van Breugel K (2007) Research developments and experimental data on dynamic concrete behaviour. In: Conference on advances in construction materials, pp 765–773
Wittmann FH (1983) Structure of concrete with respect to crack formation. Fracture Mechanics of Concrete, Elsevier Science Publishers, pp 43–74
Xu XP, Needleman A (1993) Void nucleation by inclusions debonding in a crystal matrix. Model Simul Mater Sci Eng 1:111–132